PHYSICAL REVIEW APPLIED **20,** 044070 (2023)

Optimal coupling of HoW_{10} molecular magnets to superconducting circuits near spin clock transitions

Ignacio Gimeno,[1,2] Víctor Rollano,[1,2,3,4] David Zueco,[1,2] Yan Duan,[5] Marina C. de Ory,[6]
Alicia Gomez,[6] Alejandro Gaita-Ariño,[5] Carlos Sánchez-Azqueta,[7] Thomas Astner,[8]
Daniel Granados,[9] Stephen Hill,[10] Johannes Majer,[3,4] Eugenio Coronado,[5] and
Fernando Luis[1,2,*]

[1] *Instituto de Nanociencia y Materiales de Aragón, CSIC-University of Zaragoza, Zaragoza 50009, Spain*
[2] *Departmento de Física de la Materia Condensada, Universidad de Zaragoza, Zaragoza 50009, Spain*
[3] *Hefei National Laboratory for Physical Sciences at the Microscale, University of Science and Technology of China, Hefei 230026, China*
[4] *Shanghai Branch, CAS Center for Excellence in Quantum Information and Quantum Physics, University of Science and Technology of China, Shanghai 201315, China*
[5] *Instituto de Ciencia Molecular (ICMol), Universidad de Valencia, Catedrático José Beltrán 2, Paterna 46980, Spain*
[6] *Centro de Astrobiología (CSIC-INTA), Torrejón de Ardoz, Madrid 28850, Spain*
[7] *Departamento de Física Aplicada, Universidad de Zaragoza, Zaragoza 50009, Spain*
[8] *Vienna Center for Quantum Science and Technology, Atominstitut, TU Wien, Vienna 1020, Austria*
[9] *IMDEA Nanociencia, Cantoblanco, Madrid 28049, Spain*
[10] *National High Magnetic Field Laboratory and Department of Physics, Florida State University, Tallahassee, Florida 32310, USA*

(Received 12 April 2023; revised 28 July 2023; accepted 6 October 2023; published 26 October 2023)

A central goal in quantum technologies is to maximize GT_2, where G stands for the coupling of a qubit to control and readout signals and T_2 is the qubit's coherence time. This is challenging, as increasing G (e.g., by coupling the qubit more strongly to external stimuli) often leads to deleterious effects on T_2. Here, we study the coupling of pure and magnetically diluted crystals of HoW_{10} magnetic clusters to microwave superconducting coplanar waveguides. Absorption lines give a broadband picture of the magnetic energy level scheme and, in particular, confirm the existence of level anticrossings at equidistant magnetic fields determined by the combination of crystal field and hyperfine interactions. Such "spin clock transitions" are known to shield the electronic spins against magnetic field fluctuations. The analysis of the microwave transmission shows that the spin-photon coupling also becomes maximum at these transitions. The results show that engineering spin-clock states of molecular systems offers a promising strategy to combine sizable spin-photon interactions with a sufficient isolation from unwanted magnetic noise sources.

DOI: 10.1103/PhysRevApplied.20.044070

I. INTRODUCTION

Spins embedded in solid hosts are one of the simplest and most natural choices to realize qubits, the building blocks of quantum technologies [1,2]. Their quantized spin projections can encode the qubit states, whereas operations between them can be induced via the application of microwave radiation pulses, using well-established magnetic resonance protocols. Among the different candidates, chemically designed magnetic molecules stand out for several reasons [3–8]. Besides being microscopic, and thus reproducible and intrinsically quantum, they represent the smallest structure that remains tuneable.

The ability to modify the relevant properties by adequately choosing the molecular composition and structure allows engineering the qubit spin states, energies, and coherences [9–12]. Even more, it enables scaling up computational resources within each molecule, e.g., by accommodating several different magnetic atoms in exquisitely defined coordinations [4,13–19] or by making use of multiple internal spin states [20–23].

This approach however faces the challenge of how to actually implement operations and read out the results in a realistic device and, even more, how to "wire up" different molecules into a scalable architecture. A promising

---

[*] fluis@unizar.es

technology is to exploit microwave photons in circuits [24], e.g., transmission lines for the control of spin operations and resonators for reading out the spin states and for introducing effective interactions [25–28]. Working with high-spin molecules helps maximize the spin-photon coupling, as required for such applications [25]. However, it also tends to enhance decoherence, as their interactions with fluctuating hyperfine and dipolar magnetic fields also become stronger [29,30].

A general strategy to reconcile a high qubit density with sufficient isolation is to encode each qubit in states that are robust against the dominant noise sources [31]. This idea underlies the design of the transmon superconducting qubit [32] and of several semiconducting quantum dot qubits [33]. In the case of spins, isolation from magnetic field fluctuations can be achieved by associating 0 and 1 with superposition states that arise at avoided level crossings, or "spin-clock" transitions [34–36]. Such transitions have been observed in impurity dopants in semiconductors [36] and in crystals hosting lanthanide ions [34,35], and can arise from either significant off-diagonal anisotropy terms in non-Kramers electronic spins or from hyperfine couplings in electronuclear spin systems. They have also recently been studied in magnetic molecules [11,37–41]. A paradigmatic example of the latter is provided by the sodium salt of the cluster $[\mathrm{Ho(W_5O_{18})_2}]^{9-}$ [42,43], hereafter referred to as $\mathrm{HoW_{10}}$, which consists of a single $\mathrm{Ho^{3+}}$ ion encapsulated by polyoxometalate moieties (Fig. 1). Its fourfold coordination symmetry gives rise to fourth-order off-diagonal terms in the spin Hamiltonian that strongly mix the $m_J = \pm 4$ projections of the ground electronic spin doublet. The large quantum tunneling gap $\Delta \simeq 9.1$ GHz generated by such terms, combined with the hyperfine interaction with the $I = 7/2$ spin of the Ho nucleus, gives rise to a set of level anticrossings (see Fig. 1). Near each of them, the spin coherence time T_2 is sharply enhanced [11] and the electron spin system effectively decouples from the surrounding nuclear spins [44].

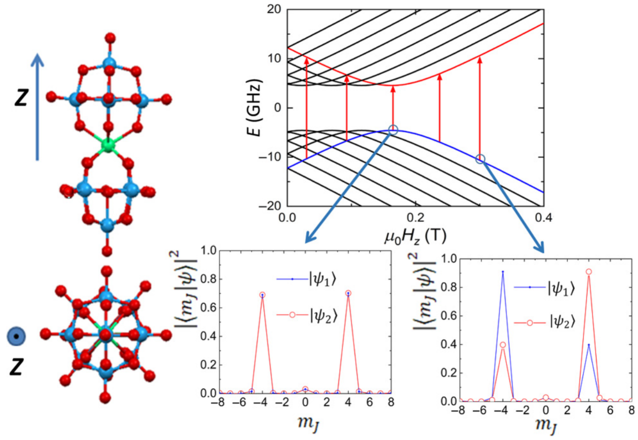

FIG. 1. Left: two views of the $\mathrm{HoW_{10}}$ cluster, showing its fourfold coordination symmetry around its anisotropy axis z. Color code: green, holmium; blue, tungsten; red, oxygen. Right: scheme of magnetic energy levels corresponding to the electronic ground doublet ($m_J = \pm 4$) of $\mathrm{HoW_{10}}$ and wave functions of two mutually avoiding levels, with nuclear spin projection $m_I = 7/2$, calculated at the indicated magnetic fields (both at and slightly off the clock transition).

In this work, we explore the coupling of $\mathrm{Ho}_x\mathrm{Y}_{1-x}\mathrm{W}_{10}$ single crystals ($x = 0.2$ and 1) to superconducting coplanar waveguides [45]. These experiments provide a direct method to investigate in detail how the spin-photon coupling evolves as a function of the magnetic field, and thus both near and far from the spin-clock transitions, and temperature. The manuscript is organized as follows. Section II provides details on the preparation of the samples, the design and fabrication of the devices, and the transmission measurements. Section III describes results obtained under different experimental conditions and discusses them with the help of input-output theory. Finally, we draw conclusions in Sec. IV.

II. EXPERIMENTAL DETAILS

A. Sample preparation and characterization

The synthesis of $\mathrm{Ho}_x\mathrm{Y}_{1-x}\mathrm{W}_{10}$ crystals followed established protocols [42]. The samples were kept in their mother solution until an experiment had to be performed, in order to protect them from degradation. The samples were characterized by means of specific heat and magnetic measurements. The results agree with those reported previously [42] and therefore confirm that $\mathrm{HoW_{10}}$ clusters have an $m_J = \pm 4$ electronic spin ground state and a sizable quantum tunneling gap Δ. Spin coherence times T_2 were determined by X-band pulse electron paramagnetic resonance (EPR) experiments on samples with Ho concentration per formula unit x ranging from 0.001 up to 0.2. Just as with measurements performed on more diluted $\mathrm{Ho}_x\mathrm{Y}_{1-x}\mathrm{W}_{10}$ samples [11], the exponential decay of the spin echo resulting from a Hahn-echo pulse sequence was fitted to extract T_2 at the given magnetic field and temperature. We find that T_2 decreases with increasing x, becoming too short to be measured for $x > 0.2$. For $x = 0.2$, $T_2 \simeq 13$ ns could only be measured near the spin clock transitions. The extrapolation of these results suggests that T_2 might become as short as 4 ns for a pure $\mathrm{HoW_{10}}$ sample.

B. Superconducting device design and fabrication

Two types of circuits hosting superconducting coplanar waveguides were employed in the microwave transmission experiments that form the core of this work. The first one consists of a 400-µm-wide central transmission line separated from two ground planes by 200-µm-wide gaps. It was fabricated by optical lithography of 100-nm-thick Nb

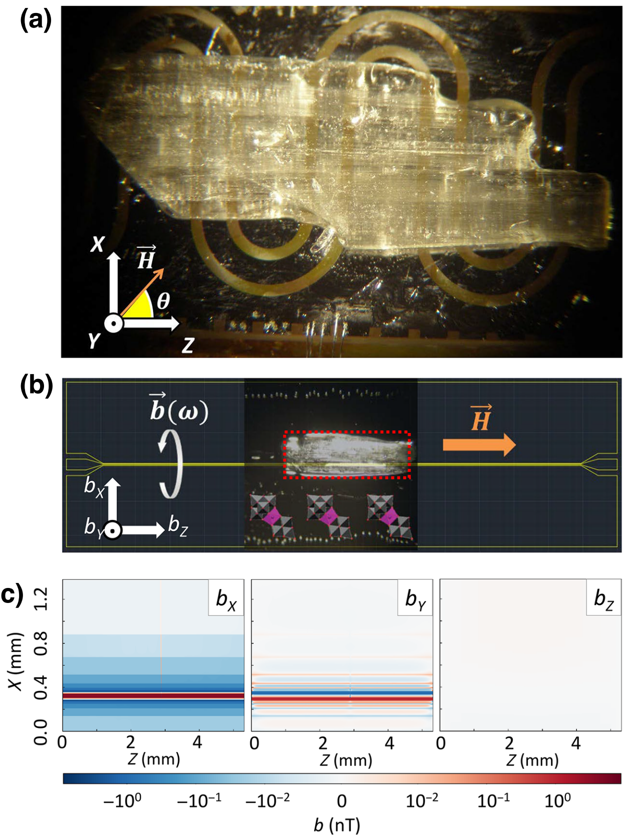

FIG. 2. (a) Image of a chip with a meanderlike 400-μm-wide superconducting transmission line hosting a single crystal of pure $\mathrm{HoW_{10}}$. This device was used for angle-dependent experiments performed at $T = 4.2$ K, with X, Y, and Z being the axes of the superconducting vector magnet that allows rotating the magnetic field *in situ*. These axes define the laboratory reference frame. (b) Sketch of a different chip, with a 35-μm-wide straight superconducting line, hosting a single crystal of $\mathrm{Ho_{0.2}Y_{0.8}W_{10}}$. This device was used in the very low-T microwave transmission measurements. The inset shows the approximate orientation of the molecules in the crystal. The reference frame shows the three components, along each of the laboratory axes, of the microwave magnetic field $\vec{b}$ generated by the line. (c) Two-dimensional plots of these three components, b_X, b_Y, and b_Z, in the X-Z region defined by the single crystal [dotted rectangle shown in panel (b)] at a constant height of 1 μm above the chip's surface. This magnetic field generates transitions between different spin states. It was calculated numerically by means of finite-element methods. The results show that $\vec{b}$ is confined within a plane perpendicular to the line (i.e., $b_Z \simeq 0$) and in a region very close to it.

films deposited by sputtering onto a single-crystalline sapphire substrate. The size of the central line and its meander shape were designed in order to match the dimensions (about $4 \times 1 \times 10$ $\mathrm{mm^3}$) of the $\mathrm{HoW_{10}}$ and $\mathrm{Ho_{0.2}Y_{0.8}W_{10}}$ single crystals that were measured at 4.2 K [Fig. 2(a)].

A second device was fabricated to optimize the coupling to the smaller size (about $1 \times 1 \times 5.5$ $\mathrm{mm^3}$), magnetically diluted $\mathrm{Ho_{0.2}Y_{0.8}W_{10}}$ crystal employed in the very low-T experiments [Fig. 2(b)]. It consists of a 35-μm-wide straight transmission line, separated from the ground planes by 20-μm-wide gaps in order to maintain a 50-Ω characteristic impedance. It was fabricated by maskless lithography and reactive ion etching techniques on a 100-nm-thick Nb film deposited by means of dc magnetron sputtering on a 275-μm-thick silicon substrate. The native oxide of the silicon wafer was previously removed using a hydrofluoric acid bath. The base pressure prior to the deposition of Nb was better than 2×10^{-8} Torr.

The magnetic field distribution generated by the microwave superconducting currents propagating via these transmission lines has been calculated using the electromagnetic simulation package SONNET [46] and finite-element simulations. Results of these simulations for the narrower straight line are shown in Fig. 2(c). The microwave magnetic field $\vec{b}$ is confined in a plane perpendicular to the line, i.e., only b_X and $b_Y \neq 0$. This information is relevant to prepare and interpret the transmission experiments, because resonant transitions between different spin states are only allowed if the microwave field has a nonzero projection along the molecular magnetic anisotropy axis z (see Sec. III below for details). Besides, its magnitude falls off quickly as one moves away from the line. This means that the experiments typically explore the coupling of a very small region of the crystal, with dimensions of about $35 \times 35 \times 5500$ $\mathrm{\mu m^3}$ along the X, Y, and Z axes. This volume contains about 8×10^{14} $\mathrm{HoW_{10}}$ molecules that couple significantly to the microwave field. Working with small crystals and sufficiently small lines, which becomes feasible at very low temperatures, helps to mitigate the effects of inhomogeneities associated with crystal twinning.

C. Microwave transmission experiments

The crystals were attached to the transmission line with apiezon N grease. Microwave transmission experiments were performed by connecting the input and output ports of the chip to a vector network analyzer that measures the transmission coefficient S_{21} for frequencies $\omega/2\pi$ ranging between 0.01 and 14 GHz. For experiments at $T = 4.2$ K, the chips were submerged in the liquid Helium bath of a cryostat equipped with a 1/1/9 T vector magnet. This set-up allows applying dc magnetic fields with amplitudes $\mu_0 H$ up to 1 T along any arbitrary direction in the X, Y, Z laboratory reference frame shown in Fig. 2(a). In these experiments, $\vec{H}$ was rotated within the X-Z plane of the device. Experiments were also performed at temperatures below 1 K, from 50 mK up to 800 mK, in order to control and optimize the thermal polarization difference ΔP_{12} between the levels involved in each resonant transition, and thus the spin-photon coupling. The chips were thermally anchored to the mixing chamber of a cryo-free dilution refrigerator, and placed at the center of an axial

1-T magnet [$\vec{H}$ was parallel to Z in this case, as shown in Fig. 2(b)]. The transmission experiments were performed as described above, with the inclusion of a set of attenuators, for a total -50 dB, in the input line and of a low noise cryogenic amplifier (gain $\simeq +35$ dB) at the $T = 4$ K stage in the output line.

In order to compensate for the decay of the waveguide transmission with increasing frequency and to enhance the contrast of those effects associated with its coupling to the spins, S_{21} was normalized. For this, we compare transmission data measured at two different magnetic fields [45]. The normalized transmission t at magnetic field H and frequency ω is given by

$$t(H,\omega) = \frac{S_{21}(H,\omega) - S_{21}(H + \Delta H,\omega)}{S_{21}^{(0)}(\omega)}, \qquad (1)$$

where $\Delta H > 0$ and $S_{21}^{(0)}$ is the transmission of the "bare" transmission line. In practice, $S_{21}^{(0)}$ is measured at a magnetic field for which all spin excitations lie outside the accessible frequency region. An example of the results obtained by this normalization method with different ΔH values is shown in Fig. 3. For ΔH smaller than the magnetic field width of a given spin transition, t approximately corresponds to the magnetic field derivative of the spin absorption line, similar to the signal detected in conventional EPR experiments. This method removes most of the "noise" (mainly associated with spurious modes coming from nonperfect impedance matching at the chip boundaries) present in the bare transmission data. For this reason, its has been used in the figures shown in Secs. III A to III D below, which aim mainly at tracking the positions of spin resonance lines. The actual absorption can also be obtained by choosing a larger ΔH but at the cost of deteriorating the signal-to-noise ratio. This method has therefore been used to estimate the spin-photon coupling (Sec. III E below), when a quantitative fit of the spin resonance absorption lines is required.

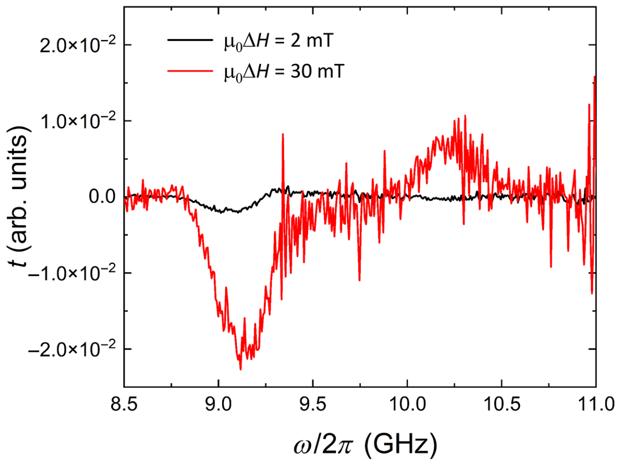

FIG. 3. Microwave transmission through a superconducting line coupled to a pure HoW$_{10}$ single crystal [see Fig. 2(a)], measured at $T = 4.2$ K and $\mu_0 H_1 = 258$ mT. The transmission has been normalized, as given by Eq. (1), by subtracting from it data measured at $H_2 = H_1 + \Delta H$, with $\mu_0\Delta H$ being either smaller (2 mT) or larger (30 mT) than the spin resonance line width. In the latter case (red solid line), the transmission minimum reflects the resonant absorption of the spins from the microwaves, whereas in the former (black solid line) it approximately corresponds to the absorption field derivative.

III. RESULTS

A. Broadband spectroscopy: field-tuned clock transitions

Figure 4 shows two-dimensional maps of the transmission through a 400-µm-wide transmission line coupled to large pure (top panel) and magnetically dilute (bottom panel) crystals. These data were measured at $T = 4.2$ K with the dc magnetic field applied along the Z axis.

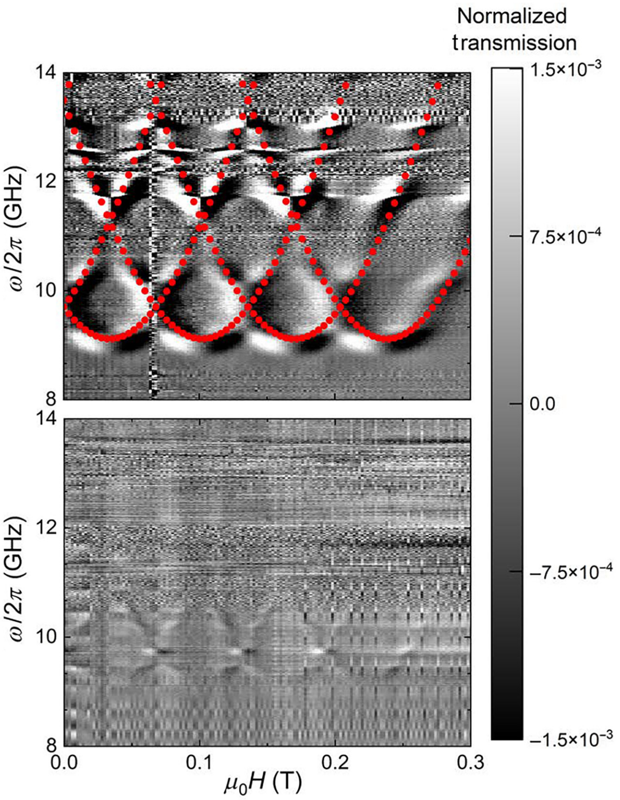

FIG. 4. Normalized transmission through a 400-µm-wide superconducting line coupled to a single crystal of pure HoW$_{10}$ (top panel) and of Ho$_{0.2}$Y$_{0.8}$W$_{10}$ (bottom panel). In both cases, the normalization [Eq. (1)] was done with $\mu_0\Delta H = 2$ mT. The experiments were performed at 4.2 K and the magnetic field was parallel to the Z laboratory axis [see Fig. 2(a)]. The dotted lines in the top panel show the frequencies of allowed spin transitions, derived from Eq. (2).

Because of the geometry of the line [see the image in Fig. 2(a) and simulations in Fig. 2(c)], the microwave magnetic field felt by the crystal was mainly confined to the *Y*-*Z* plane in this case. The data neatly show changes in transmission associated with the resonant absorption of microwave photons by the $\mathrm{HoW_{10}}$ spins. Each of these resonances corresponds to an allowed transition between two states with a different electronic spin state and the same nuclear spin state, such as those marked by vertical arrows in Fig. 1. These resonance lines then provide a complete picture of the low-lying magnetic energy levels in $\mathrm{HoW_{10}}$. In particular, they show the presence of a finite gap $\Delta \simeq 9.1$ GHz in the excitation spectrum at four different avoided level crossings. The spectroscopic patterns of pure and magnetically diluted crystals agree, save for the narrower lines observed in the latter case and the difference in absorption intensities associated with the number of spins that effectively couple to the propagating photons in each case.

B. Numerical simulation of the transmission spectra

The frequencies of the different resonances, and their dependence on the magnetic field, can be estimated from the spin Hamiltonian of an $\mathrm{Ho^{3+}}$ ion subject to the Zeeman interaction with an external magnetic field, the crystal field, and the hyperfine coupling to its $I = 7/2$ nuclear spin

$$\mathcal{H} = B_{20}\hat{O}_2^0 + B_{40}\hat{O}_4^0 + B_{60}\hat{O}_6^0 + B_{44}\hat{O}_4^4 + g_J\mu_B\vec{H}\cdot\vec{J} + AJ_zI_z. \tag{2}$$

Here, $g_J = 5/4$ is the $\mathrm{Ho^{3+}}$ Lande factor [47] and the $\hat{O}_n^m$ are the Stevens effective operators [47,48] that account for the effect that the crystal field arising from the local coordination in $\mathrm{HoW_{10}}$ has on the $J = 8$ multiplet. The magnetic anisotropy parameters $B_{20} = 0.601\ \mathrm{cm^{-1}}$, $B_{40} = 6.93 \times 10^{-3}\ \mathrm{cm^{-1}}$, $B_{60} = -5.1 \times 10^{-5}\ \mathrm{cm^{-1}}$, $B_{44} = 3.14 \times 10^{-3}\ \mathrm{cm^{-1}}$ and the hyperfine coupling constant $A = 2.77 \times 10^{-2}\ \mathrm{cm^{-1}}$ have been determined from EPR experiments on magnetically diluted samples [11,43]. Note that Eq. (2) is referenced to the molecular frame, whose axes we denote by *x*, *y*, and *z*, and that are different from the laboratory axes *X*, *Y*, and *Z*.

It follows that the ground state corresponds to the $m_J = \pm 4$ doublet, split by tunneling terms (mainly the $B_{44}\hat{O}_4^4$ term) and by hyperfine interactions. Because of the very strong uniaxial magnetic anisotropy of $\mathrm{HoW_{10}}$, avoided level crossings occur at $H_z \simeq 2m_I H_{z,1}$, with $H_{z,1} = 23$ mT for the crossing of states with nuclear spin projections $m_I = 1/2, 3/2, 5/2$, and $7/2$, respectively. The magnetic field components H_x and H_y perpendicular to the anisotropy axis have a close to negligible influence on the energy levels for magnetic fields below 300 mT, which we explore in this work. The only free parameter is then the orientation of the molecular easy axis *z* with respect to the external magnetic field, which amounts to rescaling the magnetic field axis. As shown in Fig. 4, we find good agreement with the same parameters given above. These results show that the concentrated crystals used in this work retain the same magnetic anisotropy and confirm that the strong spin tunneling, and the associated energy gap, are genuine properties of each molecule.

It is also possible to simulate the full transmission spectra. For this, we apply input-output theory to the interaction of microwave photons propagating via the transmission line with the electronic magnetic moments of the molecules. The complex transmission is then given by [49,50]

$$S_{21}^{*} = 1 - \frac{G}{G + \gamma + i(\omega_{12} - \omega)}, \tag{3}$$

where *G* is the photon-induced transition rate between spin states $|\psi_1\rangle$, with energy E_1, and $|\psi_2\rangle$, with energy E_2, (see Fig. 1), γ is the spin line width, and $\omega_{12} = (E_2 - E_1)/\hbar$ is the resonance frequency at the given magnetic field. The interaction constant *G* parameterizes the spin-photon coupling and is therefore our main interest in this work. Time-dependent perturbation theory gives the expression

$$G \simeq 2\pi g^2(\omega_{12})|\langle\psi_1|J_z|\psi_2\rangle|^2[n(\omega_{12}) + 1]\Delta P_{12}, \tag{4}$$

where $g(\omega_{12})$ is a spin-photon coupling density, which depends on the mode density in the transmission line and on geometrical factors (mainly the number of spins, their locations with respect to the circuit, and the latter's geometry), $n(\omega_{12}) = [\exp(h\omega_{12}/k_B T) - 1]^{-1}$ is the bosonic occupation number, $\Delta P_{12} = [\exp(-E_1/k_B T) - \exp(-E_2/k_B T)]/Z$ is the thermal population difference between the two levels, and *Z* is the partition function. Only the microwave field component parallel to the anisotropy axis *z* contributes to the coupling, because $\langle\psi_1|J_{x,y}|\psi_2\rangle = 0$ for any superposition of $|m_J = \pm 4\rangle$ states. This explains why *G* is determined by the matrix element of J_z.

We have performed numerical simulations of the normalized transmission amplitude based on Eqs. (1), (3), and (4) and the spin wave functions derived from the spin Hamiltonian (2). We approximate the spin-photon coupling density by the expression $g^2(\omega_{12}) \simeq \alpha\omega_{12}$, valid in the limit of one-dimensional (1D) transmission lines [51]. Here, α is an adjustable fitting parameter. The resonance line widths are of order 100–300 MHz for both the pure and magnetically diluted crystals. Electron spin resonance experiments performed on $\mathrm{Ho_{0.2}Y_{0.8}W_{10}}$ show that $T_2 \sim 0.013\ \mu$s at $T = 4.2$ K. The homogeneous broadening $1/(\pi T_2) \sim 25$ MHz is therefore much smaller than the resonance width observed in experiments, suggesting that the latter is dominated by the inhomogeneous broadening. We recognize that there are multiple sources of

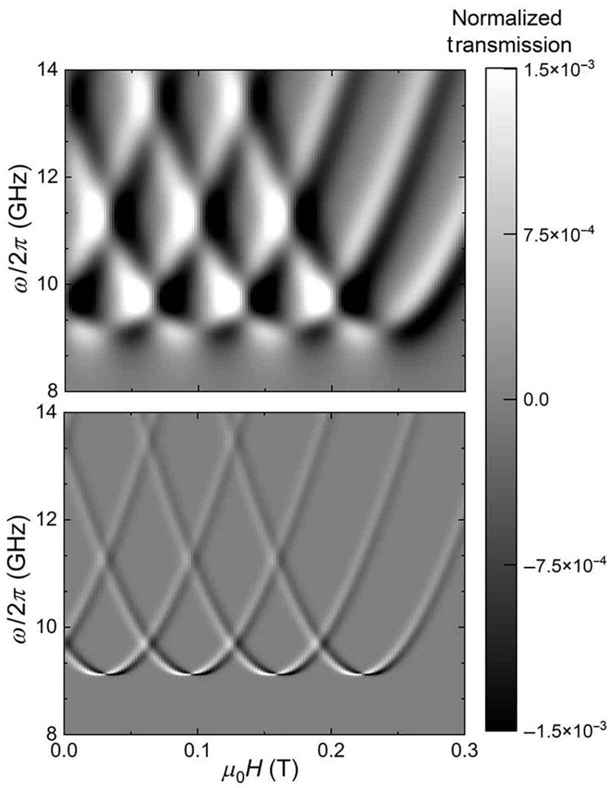

FIG. 5. Simulated 2D plots of the normalized transmission through a 400-μm-wide superconducting line coupled to a single crystal of pure HoW_{10} (top panel) and of $\mathrm{Ho}_{0.2}\mathrm{Y}_{0.8}\mathrm{W}_{10}$ (bottom panel) and for a magnetic field applied along the Z laboratory axis. The results are calculated averaging Eq. (3), with the spin-photon coupling G given by Eq. (4) and $g^2(\omega_{12}) = \alpha\omega_{12}$, over a Gaussian distribution of bias fields with a width $\sigma = 6.4$ mT for $x = 1$ and $\sigma = 2.7$ mT for $x = 0.2$. The fitting parameters were the angle $\simeq 45^\circ$ that $\vec{H}$ makes with respect to the magnetic easy axis z and the dimensionless $\alpha \simeq 3.2 \times 10^{-4}$ for HoW_{10} and $\alpha \simeq 8 \times 10^{-6}$ for $\mathrm{Ho}_{0.2}\mathrm{Y}_{0.8}\mathrm{W}_{10}$.

line broadening [11], which include dipole-dipole interactions between molecular spins and distributions in the orientations of the molecular axes and of their crystal field parameters (e.g., B_4^4 that gives rise to the tunnel splitting Δ) [11,43]. In the simulations shown in Fig. 5 their effect was introduced with Gaussian field distributions having $\sigma \simeq 6.4$ mT for $x = 1$ and $\sigma \simeq 2.7$ mT for $x = 0.2$. These parameters were chosen to give the best overall agreement with the experiments.

C. Dependence on magnetic field orientation

The experiments on the pure HoW_{10} crystal [Fig. 2(a)] were repeated for different orientations of $\vec{H}$ in the X-Z plane of the chip. This geometry allows varying the angle between $\vec{H}$ and the molecular anisotropy axis z, while minimizing effects associated with the excitation and motion of superconducting vortices.

Microwave transmission results measured for different magnetic field orientations are shown in Fig. 6. Rotating $\vec{H}$ changes the magnetic field periodicities of the avoided level crossings, but does not appreciably modify Δ. Therefore, it mainly amounts to a renormalization of the magnetic field intensity. This shows that, within the magnetic field range $\mu_0 H \leq 0.2$ T explored in these experiments, the magnetic energy levels depend almost exclusively on the projection H_z along the molecular anisotropy axis z. Therefore, the anticrossings are mainly determined by the condition $H_z = 2m_I H_{z,1}$, which requires reaching higher magnetic field strengths the more $\vec{H}$ deviates from the anisotropy axis. This agrees with the predictions of the spin Hamiltonian (2) and allows locating z. For instance, when the magnetic field forms an angle $\theta = 45^\circ$ with the X and Z laboratory axes, the pattern disappears, showing that $\vec{H}$ is then nearly orthogonal to z. By contrast, the pattern period H_1 becomes minimum for $\theta \simeq 135^\circ$, showing that $\vec{H}$ is then closest to z within the X-Z plane.

The dependence of the experimental H_1 on θ is shown in Fig. 7. Fitting H_1 versus θ data then allows estimating *in situ* the orientation of the magnetic anisotropy axis z with respect to the crystal and to the laboratory reference frame. The results are compatible with z pointing along the long molecular axis [see Figs. 1 and 2(b)].

Once the orientation of z is set, the positions of the resonances and the full transmission spectra can be calculated for any magnetic field angle. The results, shown in Fig. 6, agree very well with the experimental ones. This agreement confirms the very strong uniaxial magnetic anisotropy of HoW_{10} and provides a basis to analyze how the spin-photon coupling depends on temperature and magnetic field strength. Besides, it shows that $\vec{b}$ generated by a straight transmission line [Figs. 2(b) and 2(c)], although perpendicular to the external $\vec{B}$, has a sizable component along z. Therefore, it should also provide a nonzero spin-photon coupling. This simpler geometry [Fig. 2(b)] was then adopted for experiments performed at very low temperatures, which are discussed in what follows.

D. Broadband spectroscopy below 1 K: temperature dependence of the spin-photon coupling

The relative populations of the spin levels involved in a resonant transition influence the effective spin-photon coupling G [see Eq. (4)]. In equilibrium, this introduces a temperature dependence through the polarization parameter ΔP_{12}, which is plotted in Fig. 8. Decreasing T leads to a larger polarization provided that $k_B T$ remains sufficiently high with respect to Δ and to the hyperfine splitting of each electronic level. The fact that spin-clock transitions in HoW_{10} involve two excited levels gives rise to a maximum followed by a rapid drop in polarization.

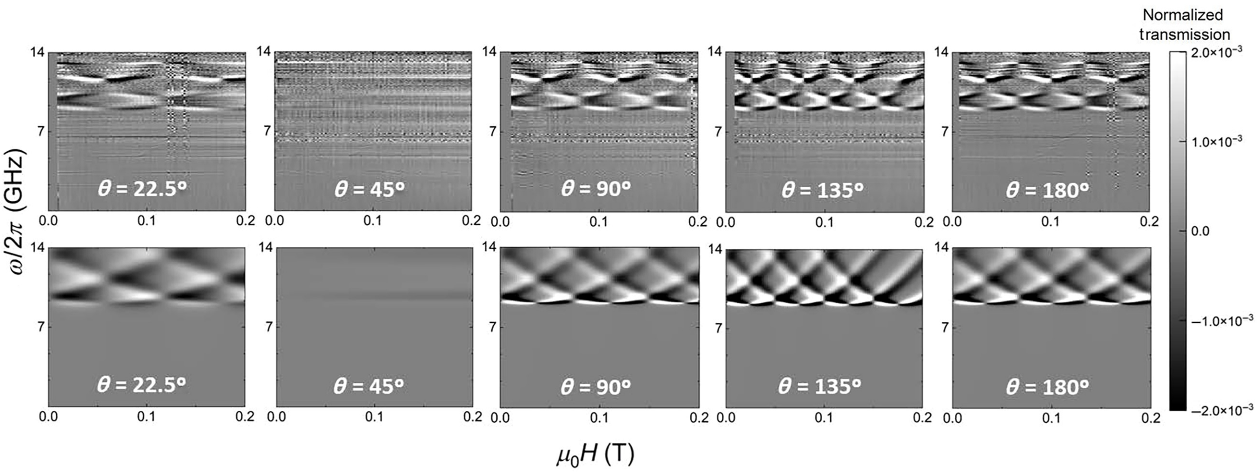

FIG. 6. Experimental (top) and simulated (bottom) normalized transmission through a 400-µm-wide superconducting line coupled to a single crystal of $\mathrm{HoW_{10}}$ for different orientations of the magnetic field. The experiments were performed at $T = 4.2$ K. The normalization of the experimental data [Eq. (1)] was done with $\mu_0 \Delta H = 2$ mT. The simulations are calculated averaging Eq. (3), with the spin-photon coupling G given by Eq. (4) and $g^2(\omega_{12}) = 3.2 \times 10^{-4}\omega_{12}$, over a $\sigma = 6.4$-mT-wide Gaussian distribution of bias fields.

This behavior is confirmed by experiments performed with the circuit shown in Fig. 2(b) on a $\mathrm{Ho_{0.2}Y_{0.8}W_{30}}$ single crystal. Transmission spectra measured at different temperatures are shown in Fig. 9. The relative intensities of the four clock transitions remain comparable to each other until, on cooling below 0.5 K, they begin to gradually fade away from right ($n = 4$) to left ($n = 1$). Numerical calculations based on Eqs. (3) and (4) are also shown in Fig. 9. They agree with this behavior. For this reason, we have chosen the data measured at $T = 0.65$ K to study the magnetic field dependence of the spin-photon coupling.

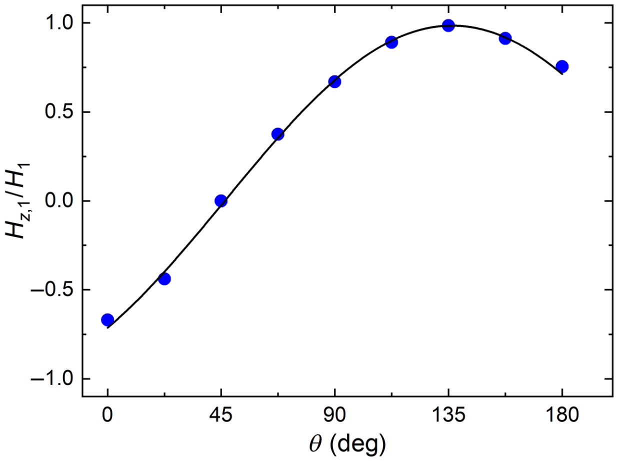

FIG. 7. Magnetic field projection along the molecular magnetic anisotropy axis z as a function of the orientation of $\vec{H}$ within the laboratory X-Z plane [see Fig. 2(a)]. Here, H_1 is the magnetic field at which the first avoided level crossing is experimentally observed (Fig. 6) and $H_{z,1} = 23$ mT is the first crossing longitudinal field derived from the spin Hamiltonian (2).

E. Magnetic field dependence of the spin-photon coupling near spin-clock transitions

Whereas the positions of the resonance lines give access to the energy level scheme, their intensities provide information on the wave functions of the involved states. An important advantage of working with open waveguides is that both the frequency and magnetic field can be varied independently of each other. It is therefore possible to monitor how the absorption intensity varies as a function of H.

Figure 10(a) shows a 2D plot of normalized transmission data measured at $T = 0.65$ K. As discussed above

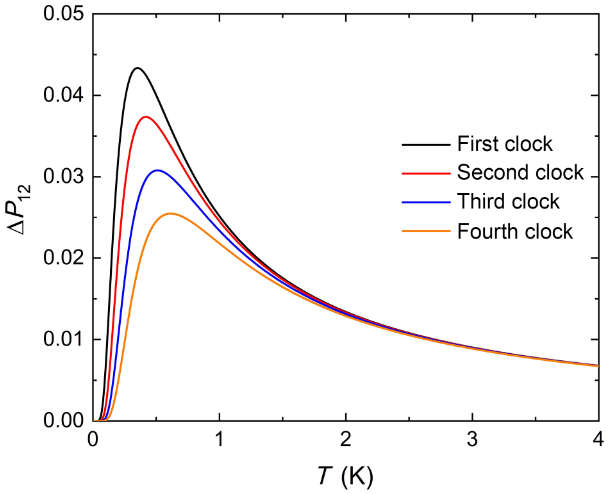

FIG. 8. Thermal equilibrium population difference between the two levels involved in each of the spin-clock transitions in $\mathrm{HoW_{10}}$.

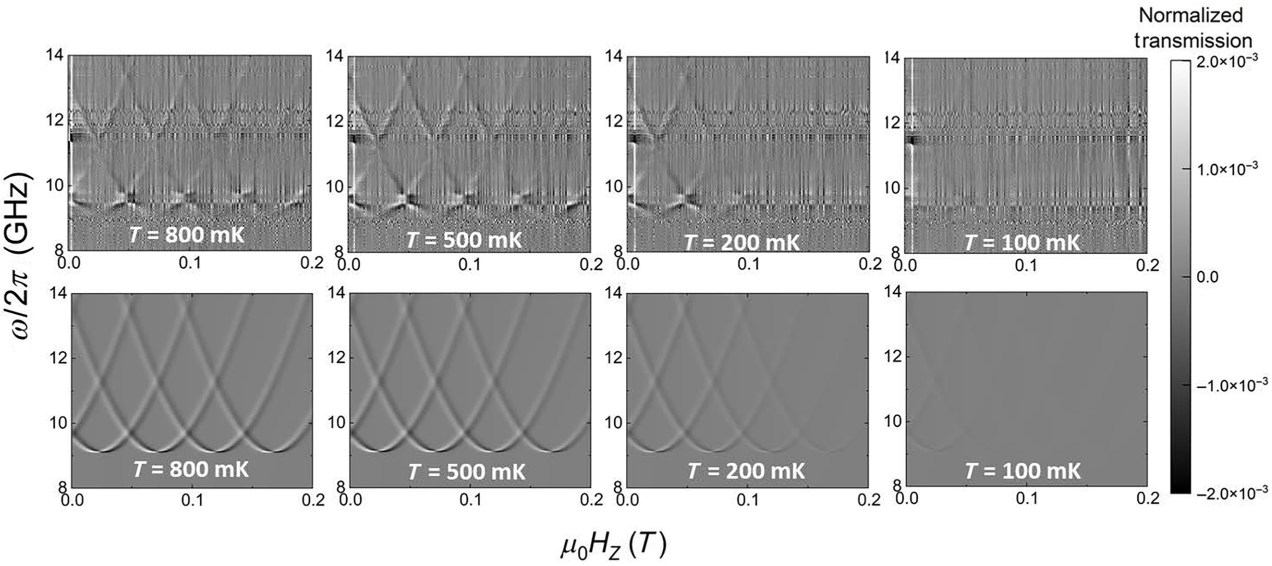

FIG. 9. Experimental (top) and simulated (bottom) normalized transmission through a 35-μm-wide superconducting line coupled to a single crystal of $\mathrm{Ho_{0.2}Y_{0.8}W_{10}}$ for different temperatures. The magnetic field was applied along the Z laboratory axis [Fig. 2(b)]. The normalization of the experimental data [Eq. (1)] was done with $\mu_0\Delta H = 1$ mT. The simulations are calculated averaging Eq. (3), with the spin-photon coupling G given by Eq. (4) and $g^2(\omega_{12}) = 1.6\times10^{-5}\omega_{12}$, over a $\sigma = 2.7$-mT-wide Gaussian distribution of bias fields.

(see also Fig. 8), this temperature provides a good compromise for the relative polarizations ΔP_{12} of all relevant spin transitions. Here, we are interested in analyzing the actual spin absorption lines, for which we have the analytical expression (3), rather than its field derivative. As we have discussed in Sec. II C, the transmission must then be normalized with data measured at a suitably separated magnetic field [see Eq. (1) and Fig. 3]. For this reason, in Fig. 10, $\mu_0\Delta H = 15$ mT, larger than the spin inhomogeneous broadening, was chosen. The minima in the normalized transmission traces [Fig. 10(b)] correspond to the absorption resonance lines at the given fields, whereas the maxima correspond to (minus) the absorption at $H + \Delta H$. Note that the relative positions of minima and maxima reflect the magnetic field slope of the $\mathrm{HoW_{10}}$ transition frequencies. Spurious resonant modes of the transmission line lead to additional transmission "bumps" that form horizontal lines in the 2D plot. In the analysis that follows, we have only considered data measured sufficiently far from such modes.

We observe that the visibility, defined as the minimum of each transmission dip, becomes enhanced on approaching each of the avoided level crossings. This phenomenon is visible in all experiments (see, e.g., Fig. 4). It can be analyzed in more detail by looking at the frequency dependence of the transmission measured at fixed magnetic fields [Fig. 10(b)]. Let us consider, for instance, the first transition that links states with nuclear spin projection $m_I = 1/2$. The maximum absorption measured near the anticrossing, at 35.4 mT and 9.3 GHz, is approximately 10 times larger than that measured away from it, at 53.7 mT and 10 GHz. The same comparison can be made, at constant H, between the intensities of different transitions that lie close or far from their respective avoided level crossings, e.g., the first and second transitions at 35.4 mT [Fig. 10(b)].

In order to get a more quantitative characterization, fits of all absorption lines have been performed with Eq. (3). The fitting parameters were the spin-photon coupling G and the line width γ, which here parameterizes the dominant inhomogeneous broadening. Examples of these fits are shown, as solid lines, in Fig. 10(b), while the results are shown in Fig. 11. The increasing difficulty in properly normalizing the transmission plus the presence of a spurious mode near 9 GHz prevents getting data right at the clock transitions. Yet, in spite of the experimental limitations, the results show that G becomes maximum at the four avoided level crossings, as can be seen in Fig. 11. Also, the line width seems to become larger on moving away from the anticrossings.

This result admits a qualitative interpretation based on Eq. (4) and on the nature of the spin transitions in $\mathrm{HoW_{10}}$ (see Fig. 1). The spin-photon coupling is largely determined by the matrix element of J_z between states with the same nuclear spin projections. The relevant subspace reduces to a two-level tunneling system [52] for which $\langle\psi_1|J_z|\psi_2\rangle \simeq |m_J|\Delta/\omega_{1,2}$, where $\omega_{1,2} = \sqrt{\Delta^2 + [2g_J m_J(H_z - 2m_I H_{z,1})]^2}$. The matrix element then inherits, although inverted, the field dependence of the level anticrossing. It reaches a maximum value

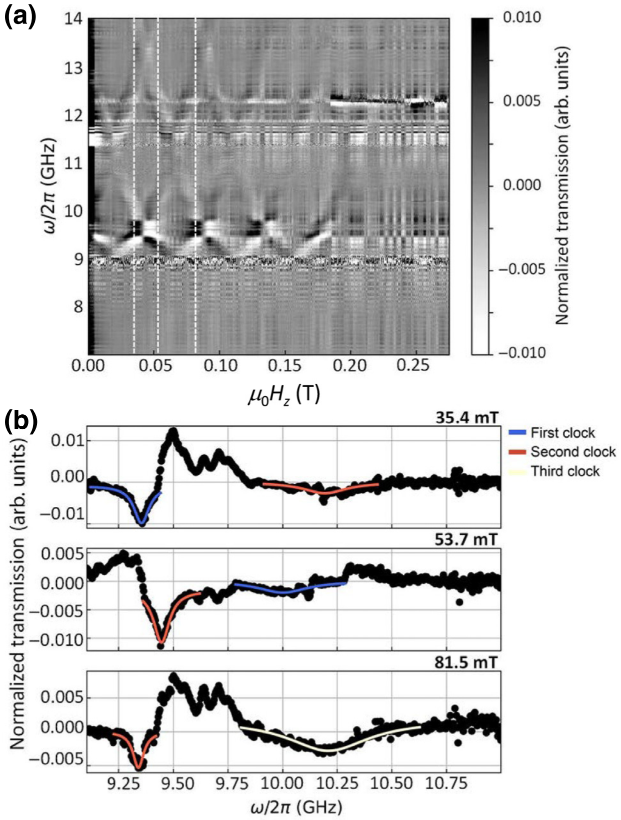

FIG. 10. (a) Two-dimensional plot of the transmission measured, at $T = 0.65$ K, on a 35-μm-wide transmission line coupled to a single crystal of $\mathrm{Ho_{0.2}Y_{0.8}W_{10}}$. The normalization of the experimental data [Eq. (1)] was done with $\mu_0 \Delta H = 15$ mT. (b) Transmission data as a function of frequency at the fields marked by vertical dotted lines in (a). The spin absorption lines correspond to the transmission dips, whereas the maxima correspond to (minus) the absorption lines of the data used in the normalization. Additional "bumps" are also visible. They arise from spurious transmission modes, which give rise to horizontal lines in the 2D plot of panel (a). The solid lines are fits, based on Eq. (3), of the different absorption resonances from which the spin-photon coupling G and the line width γ are determined.

$\langle \psi_1 | J_z | \psi_2 \rangle = |m_J|$ when the two levels come closest to each other ($\omega_{1,2} = \Delta$) and their wave functions become maximally delocalized between opposite angular momentum projections. Then, it decreases as the field moves away from H_n. Calculations performed inserting this simple expression for the matrix element into Eq. (4) reproduce quite well the experimental results, as shown in Fig. 11.

The maximum coupling $G \simeq 350$ kHz might at first seem quite modest. Yet, one has to bear in mind that we are dealing with an open transmission line and not with a resonator. Using the same theoretical basis that leads to Eqs. (3) and (4), the following relation between G and the coupling G_{res} to a cavity resonating at a given frequency ω follows [53]:

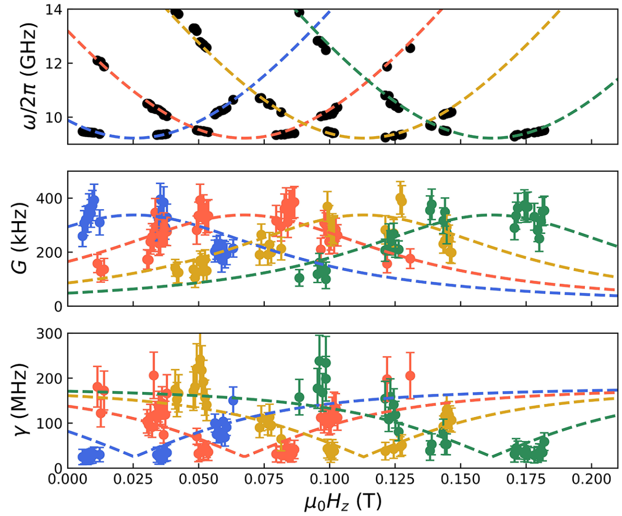

FIG. 11. Top: frequencies of the spin resonances in $\mathrm{Ho_{0.2}Y_{0.8}W_{10}}$ determined from microwave transmission experiments performed at $T = 0.65$ K. The lines are $\omega_{1,2} = \sqrt{\Delta^2 + [2 g_J m_J (H_z - 2 m_I H_{z,1})]^2}$ with $g_J = 5/4$, $m_J = 4$, $\mu_0 H_{z,1} = 23$ mT, and $m_I = 1/2$ (blue), $3/2$ (red), $5/2$ (orange), and $7/2$ (green). Avoided level crossings lead to equally spaced minima as a function of the magnetic field. Middle and bottom: spin-photon coupling G and resonance line width γ obtained from the fit of these resonances by using Eq. (3). The lines in the middle panel are calculated using Eq. (4) and the matrix element $|\langle \psi_{1)} | J_z | \psi_{2)} \rangle|^2 = m_J^2 \Delta^2 / \omega_{12}^2$, which holds for a two-level system. The lines in the bottom panel are given by $\gamma = \gamma_0 + b \partial \omega_{12} / \partial H_z$ with $\gamma_0 = 25$ MHz and $b = 4.5$ mT.

$$G_{\mathrm{res}} = \sqrt{\frac{G\omega}{\pi}}. \tag{5}$$

Using this relation, the maximum coupling to the line we measure would correspond to $G_{\mathrm{res}} \sim 80$ MHz for $\omega = 9.1$ GHz. Considering that in $\mathrm{HoW_{10}}$ the spin-photon coupling is significantly reduced by the low-spin polarization $\Delta P_{12} \leq 0.04$ (Fig. 8), this estimate compares favorably with those reported previously for other molecular [27,54–57] and inorganic [58–61] spin systems, even for crystals hosting paramagnetic lanthanide ions [57,62,63]. A reason is that our experiments involve a large number of spins [roughly $N \sim 10^{15}$ $\mathrm{HoW_{10}}$ molecules couple significantly to the microwave field in the geometry shown in Fig. 2(b)] because the line width allows working with relatively concentrated crystals. Besides, the average coupling per spin $G_1 = G_{\mathrm{res}} / \sqrt{N} \sim 2.6$ Hz is enhanced by the large ground-state spin of $\mathrm{HoW_{10}}$, for which $m_J = \pm 4$.

Concerning the line width, it is expected that γ decreases near the clock transitions. The electronic spins then become less sensitive to magnetic fields, and thus also to perturbations arising from dipolar interactions with neighbor molecules [39], hyperfine couplings to nuclear spins [44], and the misalignment of the molecular axes.

The experimental results, shown in the bottom panel of Fig. 11, confirm that spin resonances tend to narrow near the avoided level crossings. This effect can be approximately described by the expression $\gamma = \gamma_0 + b\partial\omega_{12}/\partial H_z$ [11,64], where the second term is proportional to the effective magnetic moment, which tends to vanish near a clock transition and therefore suppress the effect of bias field broadening, and the first accounts for other sources of broadening. A reasonably good fit is obtained for $b \simeq 4.5$ mT and $\gamma_0 \leqslant 25$–35 MHz. The latter value turns out to be smaller than the level broadening, of about 120 MHz, estimated from EPR experiments performed on diluted crystals and that was associated with a distribution in B_{44} [11]. The reason behind this discrepancy is not clear to us, but it might arise from a combination of the special conditions of our experiments, which are sensitive to a tiny region within a tiny crystal, and the origin of the anisotropy parameter distribution. The results suggest that the line broadening we observe is dominated by environmental magnetic fields and that their influence is reduced near the level anticrossings.

IV. CONCLUSIONS

We have explored the coupling of HoW_{10} molecular magnets to superconducting transmission waveguides. The results provide a broadband picture of the energy spectrum associated with the $m_J = \pm 4$ ground states. They confirm the existence of avoided level crossings, or spin clock transitions, at equispaced magnetic field values, determined by the magnetic anisotropy and hyperfine interactions and allow finding the orientation of the magnetic anisotropy axis.

Near each anticrossing, we find that the spin-photon coupling G becomes maximum, reflecting the maximum overlap between the two spin wave functions involved in the resonant transition. This reveals a quite unique property of spin-clock transitions. Not only do they shield spin states against magnetic field fluctuations, which leads to longer spin coherence times T_2 [11], but they also optimize their coupling to external radiation fields. This enhancement is quite remarkable since the transition linking $m_J = \pm 4$ states would be strictly forbidden for vanishing Δ. By contrast, when $\Delta \neq 0$, the coupling to photons becomes enhanced in qubits that, like HoW_{10}, are characterized by a large effective ground-state spin, since $G \propto m_J^2$ near the anticrossing. This property makes spin clock transitions promising for developing fast and robust qubits out of high-spin ($S > 1/2$) magnetic molecules, e.g., those based on lanthanide ions. The limitation imposed by the difficulty of tuning ω_{12} with a magnetic field can be compensated by exploiting electric fields, whose effect becomes maximum near the anticrossings [65].

The experimental scheme used in this work is also a quite standard tool to control spin qubits on a chip, as has been shown by experiments performed on N-V^- centers in diamond [66] and impurity spins in silicon [67]. Our results show a simple method to maximize the Rabi frequencies of single-qubit operations on high-spin systems with suitable magnetic anisotropies. Besides, this scheme can be integrated with circuit QED architectures, e.g., with the application of superconducting resonators to readout the spin states [26,28]. The enhancement of the spin-photon coupling found here should also lead to larger dispersive shifts, and thus improve the visibility of different spin states [68]. This is especially relevant when dealing with molecular spin qudits, e.g., those based on Gd^{3+} ions [20]. Even though Gd^{3+} is a Kramers ion, the combination of nondiagonal magnetic anisotropy terms and adequately oriented external magnetic fields also leads to avoided level crossings in these systems. Exploiting the enhanced spin-photon coupling near them might then allow reaching the high cooperativity regime needed to resolve their multiple spin states even with non-too-diluted crystals, and therefore provide a suitable platform for proof-of-concept implementations of qudit-based algorithms [28,69,70].

ACKNOWLEDGMENTS

This work has received support from Grants No. RTI2018-096075-A-C21, No. PID2019-105552RB-C41, No. PID2019-105552RB-C44, No. P2018/NMT-4291 No. TEC2SPACE-CM, No. TED2021-131447B-C21, No. TED2021-131447B-C22, No. CEX2019-000919-M and No. CEX2020-001039-S, funded by MCIN/AEI/10.13039/501100011033, ERDF "A way of making Europe" and ESF "Investing in your future", and from the Gobierno de Aragón Grant No. E09-17R-Q-MAD. We also acknowledge funding from the European Union Horizon 2020 research and innovation programme through FET-OPEN Grant No. FATMOLS-No862893, ERC advanced Grant No. Mol-2D-No788222, ERC consolidator Grant No. DECRESIM-No647301, and HORIZON-MSCA-2021 Grant No. HyQuArch-No101064707. This study also forms part of the Advanced Materials and Quantum Communication programmes, supported by MCIN with funding from European Union NextGenerationEU (PRTR-C17.I1), by Gobierno de Aragón, by Generalitat Valenciana, and by CSIC (PTI001). S.H. acknowledges support from the US Department of Energy (DE-SC0020260). Work done at the National High Magnetic Field Laboratory is supported by the US National Science Foundation (DMR-1644779 and DMR-2128556) and the State of Florida.

[1] S. Bertaina, S. Gambarelli, A. Tkachuk, I. N. Kurkin, B. Malkin, A. Stepanov, and B. Barbara, Rare-earth solid-state qubits, Nat. Nanotechnol. **2**, 39 (2007).

[2] D. D. Awschalom, L. C. Bassett, A. S. Dzurak, E. L. Hu, and J. R. Petta, Quantum spintronics: Engineering and

manipulating atom-like spins in semiconductors, Science **339**, 1174 (2013).

[3] F. Troiani and M. Affronte, Molecular spins for quantum information technologies, Chem. Soc. Rev. **40**, 3119 (2011).

[4] G. Aromí, D. Aguilà, P. Gamez, F. Luis, and O. Roubeau, Design of magnetic coordination complexes for quantum computing, Chem. Soc. Rev. **41**, 537 (2012).

[5] A. Gaita-Ariño, F. Luis, S. Hill, and E. Coronado, Molecular spins for quantum computation, Nat. Chem. **11**, 301 (2019).

[6] M. Atzori and R. Sessoli, The second quantum revolution: Role and challenges of molecular chemistry, J. Am. Chem. Soc. **141**, 11339 (2019).

[7] M. R. Wasielewski, M. D. E. Forbes, N. L. Frank, K. Kowalski, G. D. Scholes, J. Yuen-Zhou, M. A. Baldo, D. E. Freedman, R. H. Goldsmith, T. Goodson III, M. L. Kirk, J. K. McCusker, J. P. Ogilvie, D. A. Shultz, S. Stoll, and K. B. Whaley, Exploiting chemistry and molecular systems for quantum information science, Nat. Rev. Chem. **4**, 490 (2020).

[8] S. Carretta, D. Zueco, A. Chiesa, A. Gómez-León, and F. Luis, A perspective on scaling up quantum computation with molecular spins, Appl. Phys. Lett. **118**, 240501 (2021).

[9] M. J. Martínez-Pérez, S. Cardona-Serra, C. Schlegel, F. Moro, P. J. Alonso, H. Prima-García, J. M. Clemente-Juan, M. Evangelisti, A. Gaita-Ariño, J. Sesé, J. van Slageren, E. Coronado, and F. Luis, Gd-based single-ion magnets with tunable magnetic anisotropy: Molecular design of spin qubits, Phys. Rev. Lett. **108**, 247213 (2012).

[10] C. J. Wedge, G. A. Timco, E. T. Spielberg, R. E. George, F. Tuna, S. Rigby, E. J. L. McInnes, R. E. P. Winpenny, S. J. Blundell, and A. Ardavan, Chemical engineering of molecular qubits, Phys. Rev. Lett. **108**, 107204 (2012).

[11] M. Shiddiq, D. Komijani, Y. Duan, A. Gaita-Ariño, E. Coronado, and S. Hill, Enhancing coherence in molecular spin qubits via atomic clock transitions, Nature **531**, 348 (2016).

[12] S. L. Bayliss, P. Deb, D. W. Laorenza, M. Onizhuk, G. Galli, D. E. Freedman, and D. D. Awschalom, Enhancing spin coherence in optically addressable molecular qubits through host-matrix control, Phys. Rev. X **12**, 031028 (2022).

[13] F. Luis, A. Repollés, M. J. Martínez-Pérez, D. Aguilà, O. Roubeau, D. Zueco, P. J. Alonso, M. Evangelisti, A. Camón, J. Sesé, L. A. Barrios, and G. Aromí, Molecular prototypes for spin-based CNOT and SWAP quantum gates, Phys. Rev. Lett. **107**, 117203 (2011).

[14] D. Aguilà, L. A. Barrios, V. Velasco, O. Roubeau, A. Repollés, P. J. Alonso, J. Sesé, S. J. Teat, F. Luis, and G. Aromí, Heterodimetallic [LnLn′] lanthanide complexes: Toward a chemical design of two-qubit molecular spin quantum gates, J. Am. Chem. Soc. **136**, 14215 (2014).

[15] J. Ferrando-Soria, E. Moreno-Pineda, A. Chiesa, A. Fernández, S. A. Magee, S. Carretta, P. Santini, I. J. Vitorica-Yrezabal, F. Tuna, G. A. Timco, E. J. L. McInnes, and R. E. P. Winpenny, A modular design of molecular qubits to implement universal quantum gates, Nat. Commun. **7**, 11377 (2016).

[16] A. Fernández, J. Ferrando-Soria, E. Moreno-Pineda, F. Tuna, I. J. Vitorica-Yrezabal, C. Knappke, J. Ujma, C. A. Muryn, G. A. Timco, P. E. Barran, A. Ardavan, and R. E. P. Winpenny, Making hybrid [*n*]-rotaxanes as supramolecular arrays of molecular electron spin qubits, Nat. Commun. **7**, 10240 (2016).

[17] F. Luis, P. J. Alonso, O. Roubeau, V. Velasco, D. Zueco, D. Aguilà, J. I. Martínez, L. A. Barrios, and G. Aromí, A dissymmetric [Gd_2] coordination molecular dimer hosting six addressable spin qubits, Commun. Chem. **3**, 176 (2020).

[18] S. J. Selena J. Lockyer, A. Chiesa, A. Brookfield, G. A. Timco, G. F. S. Whitehead, E. J. L. McInnes, S. Carretta, and R. E. P. Winpenny, Five-spin supramolecule for simulating quantum decoherence of Bell states, J. Am. Chem. Soc. **144**, 16086 (2022).

[19] D. Ranieri, F. Santanni, A. Privitera, A. Albino, E. Salvadori, M. Chiesa, F. Totti, L. Sorace, and R. Sessoli, An exchange coupled meso–meso linked vanadyl porphyrin dimer for quantum information processing, Chem. Sci. **14**, 61 (2023).

[20] M. D. Jenkins, Y. Duan, B. Diosdao, J. J. García-Ripoll, A. Gaita-Ariño, C. Giménez-Saiz, P. J. Alonso, E. Coronado, and F. Luis, Coherent manipulation of three-qubit states in a molecular single-ion magnet, Phys. Rev. B **95**, 064423 (2017).

[21] C. Godfrin, A. Ferhat, R. Ballou, S. Klyatskaya, M. Ruben, W. Wernsdorfer, and F. Balestro, Operating quantum states in single magnetic molecules: Implementation of Grover's quantum algorithm, Phys. Rev. Lett. **119**, 187702 (2017).

[22] E. Moreno-Pineda, C. Godfrin, F. Balestro, W. Wernsdorfer, and M. Ruben, Molecular spin qudits for quantum algorithms, Chem. Soc. Rev. **47**, 501 (2018).

[23] R. Hussain, G. Allodi, A. Chiesa, E. Garlatti, D. Mitcov, A. Konstantatos, K. S. Pedersen, R. De Renzi, S. Piligkos, and S. Carretta, Coherent manipulation of a molecular Ln-based nuclear qudit coupled to an electron qubit, J. Am. Chem. Soc. **140**, 9814 (2018).

[24] A. Blais, A. L. Grimsmo, S. M. Girvin, and A. Wallraff, Circuit quantum electrodynamics, Rev. Mod. Phys. **93**, 025005 (2021).

[25] M. D. Jenkins, T. Hümmer, M. J. Martínez-Pérez, J. J. García-Ripoll, D. Zueco, and F. Luis, Coupling single-molecule magnets to quantum circuits, New J. Phys. **15**, 095007 (2013).

[26] M. D. Jenkins, D. Zueco, O. Roubeau, G. Aromi, J. Majer, and F. Luis, A scalable architecture for quantum computation with molecular nanomagnets, Dalton Trans. **45**, 16682 (2016).

[27] C. Bonizzoni, A. Ghirri, and M. Affronte, Coherent coupling of molecular spins with microwave photons in planar superconducting resonators, Adv. Phys. X **3**, 1435305 (2018).

[28] A. Chiesa, S. Roca, S. Chicco, M. de Ory, A. Gómez-León, A. Gomez, D. Zueco, F. Luis, and S. Carretta, Blueprint for a molecular-spin quantum processor, Phys. Rev. Appl. **19**, 064060 (2023).

[29] A. Morello, P. C. E. Stamp, and I. S. Tupitsyn, Pairwise decoherence in coupled spin qubit networks, Phys. Rev. Lett. **97**, 207206 (2006).

[30] L. Escalera-Moreno, A. Gaita-Ariño, and E. Coronado, Decoherence from dipolar interspin interactions in molecular spin qubits, Phys. Rev. B **100**, 064405 (2019).

[31] D. A. Lidar, I. L. Chuang, and K. B. Whaley, Decoherence-free subspaces for quantum computation, Phys. Rev. Lett. **81**, 2594 (1998).

[32] J. Koch, T. M. Yu, J. Gambetta, A. A. Houck, D. I. Schuster, J. Majer, A. Blais, M. H. Devoret, S. M. Girvin, and R. J. Schoelkopf, Charge-insensitive qubit design derived from the Cooper pair box, Phys. Rev. A **76**, 042319 (2007).

[33] G. Burkard, T. D. Ladd, J. M. Nichol, A. Pan, and J. R. Petta, Semiconductor spin qubits, Rev. Mod. Phys. **95**, 025003 (2023).

[34] J. J. Longdell, A. L. Alexander, and M. J. Sellars, Characterization of the hyperfine interaction in europium-doped yttrium orthosilicate and europium chloride hexahydrate, Phys. Rev. B **74**, 195101 (2006).

[35] D. L. McAuslan, J. G. Bartholomew, M. J. Sellars, and J. J. Longdell, Reducing decoherence in optical and spin transitions in rare-earth-metal-ion-doped materials, Phys. Rev. A **85**, 032339 (2012).

[36] G. Wolfowicz, A. M. Tyryshkin, R. E. George, H. Riemann, N. V. Abrosimov, P. Becker, H.-J. Pohl, M. L. Thewalt, S. A. Lyon, and J. J. L. Morton, Atomic clock transitions in silicon-based spin qubits, Nat. Nanotechnol. **8**, 561 (2013).

[37] J. M. Zadrozny, A. T. Gallagher, T. D. Harris, and D. E. Freedman, A porous array of clock qubits, J. Am. Chem. Soc. **139**, 7089 (2017).

[38] C. A. Collett, K.-I. Ellers, N. Russo, K. R. Kittilstved, G. A. Timco, R. E. P. Winpenny, and J. R. Friedman, A clock transition in the Cr$_7$Mn molecular nanomagnet, Magnetochemistry **5**, 4 (2019).

[39] M. Rubín-Osanz, F. Lambert, F. Shao, E. Rivière, R. Guillot, N. Suaud, N. Guihéry, D. Zueco, A.-L. Barra, T. Mallah, and F. Luis, Chemical tuning of spin clock transitions in molecular monomers based on nuclear spin-free Ni(II), Chem. Sci. **12**, 5123 (2021).

[40] I. Gimeno, A. Urtizberea, J. Román-Roche, D. Zueco, A. Camón, P. J. Alonso, O. Roubeau, and F. Luis, Broad-band spectroscopy of a vanadyl porphyrin: A model electronuclear spin qudit, Chem. Sci. **12**, 5621 (2021).

[41] K. Kundu, J. R. White, S. A. Moehring, J. M. Yu, J. W. Ziller, F. Furche, W. J. Evans, and S. Hill, A 9.2-GHz clock transition in a Lu(II) molecular spin qubit arising from a 3,467-MHz hyperfine interaction, Nat. Chem. **14**, 392 (2022).

[42] M. A. AlDamen, S. Cardona-Serra, J. M. Clemente-Juan, E. Coronado, A. Gaita-Ariño, C. Martí-Gastaldo, F. Luis, and O. Montero, Mononuclear lanthanide single molecule magnets based on the polyoxometalates $[\mathrm{Ln}(\mathrm{W}_5\mathrm{O}_{18})_2]^{9-}$ and $[\mathrm{Ln}(\beta_2\text{-}\mathrm{SiW}_{11}\mathrm{O}_{39})_2]^{13-}(\mathrm{Ln} = \mathrm{Tb, Dy, Ho, Er, Tm,}$ and Yb), Inorg. Chem. **48**, 3467 (2009).

[43] S. Ghosh, S. Datta, L. Friend, S. Cardona-Serra, A. Gaita-Ariño, E. Coronado, and S. Hill, Multi-frequency EPR studies of a mononuclear holmium single-molecule magnet based on the polyoxometalate $\mathrm{Ho}(\mathrm{W}_5\mathrm{O}_{18})_2{}^{9-}$, Dalton Trans. **41**, 13697 (2012).

[44] K. Kundu, J. Chen, S. Hoffman, J. Marbey, D. Komijani, Y. Duan, A. Gaita-Ariño, J. Stanton, X. Zhang, C. Hai-Ping, and S. Hill, Electron-nuclear decoupling at a spin clock transition, Commun. Phys. **6**, 38 (2023).

[45] C. Clauss, D. Bothner, D. Koelle, R. Kleiner, L. Bogani, M. Scheffler, and M. Dressel, Broadband electron spin resonance from 500 MHz to 40 GHz using superconducting coplanar waveguides, Appl. Phys. Lett. **102**, 162601 (2013).

[46] Sonnet Software Inc., Sonnet User's Guide, Release 18. [Online] https://www.sonnetsoftware.com/support/.

[47] A. Abragam and B. Bleaney, *Electron Paramagnetic Resonance of Transition Ions*, Oxford Classic Texts in the Physical Sciences (OUP Oxford, 2012). https://books.google.es/books?id=ASNoAgAAQBAJ.

[48] K. W. H. Stevens, Matrix elements and operator equivalents connected with the magnetic properties of rare earth ions, Proc. Phys. Soc. A **65**, 209 (1952).

[49] S. Fan, U. E. KocabaS, and J. Shen, Input-output formalism for few-photon transport in one-dimensional nanophotonic waveguides coupled to a qubit, Phys. Rev. A **82**, 063821 (2010).

[50] E. Sánchez-Burillo, L. Martín-Moreno, J. J. García-Ripoll, and D. Zueco, Full two-photon down-conversion of a single photon, Phys. Rev. A **94**, 053814 (2016).

[51] J. J. García-Ripoll, *Quantum Information and Quantum Optics with Superconducting Circuits* (Cambridge University Press, Cambridge, 2022).

[52] A. J. Leggett, S. Chakravarty, A. T. Dorsey, M. P. A. Fisher, A. Garg, and W. Zwerger, Dynamics of the dissipative two-state system, Rev. Mod. Phys. **59**, 1 (1987).

[53] T. Hümmer, F. J. García-Vidal, L. Martín-Moreno, and D. Zueco, Weak and strong coupling regimes in plasmonic QED, Phys. Rev. B **87**, 115419 (2013).

[54] A. Ghirri, C. Bonizzoni, F. Troiani, N. Buccheri, L. Beverina, A. Cassinese, and M. Affronte, Coherently coupling distinct spin ensembles through a high-T_c superconducting resonator, Phys. Rev. A **93**, 063855 (2016).

[55] M. Mergenthaler, J. Liu, J. J. Le Roy, N. Ares, A. L. Thompson, L. Bogani, F. Luis, S. J. Blundell, T. Lancaster, A. Ardavan, G. A. D. Briggs, P. J. Leek, and E. A. Laird, Strong coupling of microwave photons to antiferromagnetic fluctuations in an organic magnet, Phys. Rev. Lett. **119**, 147701 (2017).

[56] C. Bonizzoni, A. Ghirri, M. Atzori, L. Sorace, R. Sessoli, and M. Affronte, Coherent coupling between vanadyl phthalocyanine spin ensemble and microwave photons: towards integration of molecular spin qubits into quantum circuits, Sci. Rep. **7**, 13096 (2017).

[57] V. Rollano, M. C. de Ory, C. D. Buch, M. Rubín-Osanz, D. Zueco, C. Sánchez-Azqueta, A. Chiesa, D. Granados, S. Carretta, A. Gomez, S. Piligkos, and F. Luis, High cooperativity coupling to nuclear spins on a circuit quantum electrodynamics architecture, Commun. Phys. **5**, 246 (2022).

[58] Y. Kubo, F. R. Ong, P. Bertet, D. Vion, V. Jacques, D. Zheng, A. Dréau, J.-F. Roch, A. Auffeves, F. Jelezko, J. Wrachtrup, M. F. Barthe, P. Bergonzo, and D. Esteve, Strong coupling of a spin ensemble to a superconducting resonator, Phys. Rev. Lett. **105**, 140502 (2010).

[59] D. I. Schuster, A. P. Sears, E. Ginossar, L. DiCarlo, L. Frunzio, J. J. L. Morton, H. Wu, G. A. D. Briggs, B. B. Buckley, D. D. Awschalom, and R. J. Schoelkopf, High-cooperativity coupling of electron-spin ensembles to superconducting cavities, Phys. Rev. Lett. **105**, 140501 (2010).

[60] H. Wu, R. E. George, J. H. Wesenberg, K. Mølmer, D. I. Schuster, R. J. Schoelkopf, K. M. Itoh, A. Ardavan, J. J. L. Morton, and G. A. D. Briggs, Storage of multiple coherent microwave excitations in an electron spin ensemble, Phys. Rev. Lett. **105**, 140503 (2010).

[61] R. Amsüss, C. Koller, T. Nöbauer, S. Putz, S. Rotter, K. Sandner, S. Schneider, M. Schramböck, G. Steinhauser, H. Ritsch, J. Schmiedmayer, and J. Majer, Cavity QED with magnetically coupled collective spin states, Phys. Rev. Lett. **107**, 060502 (2011).

[62] S. Probst, H. Rotzinger, S. Wünsch, P. Jung, M. Jerger, M. Siegel, A. V. Ustinov, and P. A. Bushev, Anisotropic rare-earth spin ensemble strongly coupled to a superconducting resonator, Phys. Rev. Lett. **110**, 157001 (2013).

[63] A. Tkalčec, S. Probst, D. Rieger, H. Rotzinger, S. Wünsch, N. Kukharchyk, A. D. Wieck, M. Siegel, A. V. Ustinov, and P. Bushev, Strong coupling of an Er3+-doped $YAlO_3$ crystal to a superconducting resonator, Phys. Rev. B **90**, 075112 (2014).

[64] S. J. Balian, G. Wolfowicz, J. J. L. Morton, and T. S. Monteiro, Quantum-bath-driven decoherence of mixed spin systems, Phys. Rev. B **89**, 045403 (2014).

[65] J. Liu, J. Mrozek, A. Ullah, Y. Duan, J. J. Baldoví, E. Coronado, A. Gaita-Ariño, and A. Ardavan, Quantum coherent spin–electric control in a molecular nanomagnet at clock transitions, Nat. Phys. **17**, 1205 (2021).

[66] R. Hanson, V. V. Dobrovitski, A. E. Feiguin, O. Gywat, and D. D. Awschalom, Coherent dynamics of a single spin interacting with an adjustable spin bath, Science **320**, 352 (2008).

[67] J. J. Pla, K. Y. Tan, J. P. Dehollain, W. H. Lim, J. J. L. Morton, D. N. Jamieson, A. S. Dzurak, and A. Morello, A single-atom electron spin qubit in silicon, Nature **489**, 541 (2012).

[68] A. Gómez-León, F. Luis, and D. Zueco, Dispersive readout of molecular spin qudits, Phys. Rev. Appl. **17**, 064030 (2022).

[69] A. Chiesa, E. Macaluso, F. Petiziol, S. Wimberger, P. Santini, and S. Carretta, Molecular nanomagnets as qubits with embedded quantum-error correction, J. Phys. Chem. Lett. **11**, 8610 (2020).

[70] M. Chizzini, L. Crippa, L. Zaccardi, E. Macaluso, S. Carretta, A. Chiesa, and P. Santini, Quantum error correction with molecular spin qudits, Phys. Chem. Chem. Phys. **24**, 20030 (2022).